Title

Uncovering the True Active Sites in Ni—N—C Catalysts for CO2 Electroreduction

Journal

Journal of the American Chemical Society, 147(42)

ISSN

0002-7863

Authors

Han, Yulan
Wei, Yu
Goswami, Anubhav
et al.

Publication Date

2025-10-22

DOI

10.1021/jacs.5c12847

Uncovering the True Active Sites in Ni-N-C Catalysts for CO_2 Electroreduction

Yulan Han,[1] Yu Wei,[1] Anubhav Goswami,[1] Anastassia Alexandrova,[1,2]*

[1]Department of Chemistry and Biochemistry, [2]Department of Materials Science and Engineering, University of California, Los Angeles, Los Angeles, CA 90095, USA

[*]Corresponding author emails: alexandrova@g.ucla.edu,

Abstract

Understanding and designing active sites in single-atom catalysts (SACs) requires going beyond static models to capture their dynamic evolution under realistic electrochemical conditions. Here, we develop an integrated theoretical framework that accounts for operational conditions, by combining grand canonical density functional theory (GC-DFT) with machine learning-accelerated sampling to uncover structure-activity-stability relationships in Ni-N-C SACs for CO_2 reduction reaction (CO_2RR). A library of NiN_xC_{4-x} (x = 0-4) motifs—representing coordination defects likely formed during high-temperature synthesis—was systematically evaluated. Under working conditions, these sites were found to undergo hydrogenation, and $NiN_3C_1\_H_1$ was identified as the most probable active site. At reducing potentials, hydrogen adsorbs spontaneously at C-Ni bridge sites rather than Ni top sites, while subsurface hydrogen facilitates bent CO_2 adsorption crucial for activation. High CO_2RR selectivity toward CO arises from site separation: Ni centers drive CO_2RR, while the hydrogen evolution reaction (HER) occurs at C-Ni bridge or N sites, and from thermodynamic suppression of HER at moderate hydrogen coverage. At more negative potentials, a shift in the CO_2RR rate-determining process (RDP), and Ni out-of-surface displacement induced by co-adsorption of H and H_2O, jointly reduce activity and selectivity. Thus, both the high CO_2RR selectivity of Ni-N-C catalysts, and its reversal with more negative potentials, can be rationalized by accounting for hydrogenated surfaces. This highlights

the necessity of modeling realistic, in situ conditions. This framework provides generalizable insight into dynamic active sites in SACs, offering guidance for the rational design of active and robust catalysts across diverse electrochemical reactions.

Introduction

Single-atom catalysts (SACs) have emerged as a transformative class of materials in heterogeneous electrocatalysis, offering maximal atom utilization alongside high catalytic activity.[1–6] Their apparent structural simplicity, consisting of isolated metal atoms anchored on supports such as nitrogen-doped graphene, has enabled rigorous mechanistic interrogation using both experimental and computational approaches, enabling detailed correlation between atomic-scale structure and catalytic function. These investigations have provided valuable guidelines for designing active sites toward key reactions such as CO_2 reduction reaction (CO_2RR),[7–12] oxygen reduction reaction (ORR),[13–16] and hydrogen evolution reaction (HER).[17–19]

However, despite the conceptual clarity offered by idealized models of these systems, the real catalytic environment is far more complex and dynamic, often rendering insights from well-defined structures inapplicable to real catalysts. First, unlike molecular catalysts with explicit MN_4(M = metal) coordination, M-N-C materials synthesized under high-temperature conditions exhibit globally implicit and structurally heterogeneous motifs due to the lack of precise control at the molecular level during synthesis. As a result, a diverse ensemble of configurations, such as MN_x (x = 1-4), MC_x species, and defects within the carbon matrix can be formed, making it challenging to unambiguously identify the true active site.[20–23] Second, under operating conditions, the catalyst surface is dynamically reshaped by the applied potential, electrolyte environment and reaction intermediates/products. These factors can induce protonation,[7,24,25] hydroxylation,[26,27] or adsorbate binding,[28–30] thereby continuously altering the coordination geometry and electronic properties of the active site. These local changes can also impact the stability of metal atoms, leading to restructuring, migration, or detachment of metal centers and in some cases, the formation of metal

clusters.[24,29,31,32] As a result, a central question remains unresolved: what is the true active site of SACs under operating conditions? Addressing this challenge is essential for developing predictive models of catalytic performance and guiding the rational design of more robust and active catalysts.

Here, we focus on Ni-N-C systems, a widely studied class of electrocatalysts known for their high activity and selectivity toward CO_2RR.[12,33–36] Despite their remarkable performance, the nature of the true active sites remains elusive. First, multiple local coordination environments, viz. NiN_4[37-39], NiN_3C_1[33], NiN_2C_2[34,40], NiN_1C_3[41], NiN_3[42], NiN_2V_2[43] (V = coordination vacancy of Ni centers), and NiN_3V_1,[44] have been proposed, yet it remains unclear which configuration is catalytically most relevant. Second, the origin of their intrinsically high CO_2RR selectivity cannot be satisfactorily explained by conventional static models. For instance, idealized NiN_4 sites exhibit prohibitively high barriers for *COOH formation[35] while others show high HER activity due to moderate H* adsorption on C-Ni bridge sites.[37] Third, while experiments based on Tafel slopes generally support *COOH formation as the rate-determining step[35], theoretical predictions vary considerably, with some identifying CO_2 adsorption ,*COOH formation, or CO desorption as rate-limiting.[12,21,45] Fourth, a drop in CO selectivity at more negative potentials is frequently observed[34,46], yet its mechanistic origin remains ambiguous: a shift in the rate determining process (RDP), enhanced competing HER kinetics, or potential-induced structural reconstruction, limited CO_2 mass transport[47] have all been proposed as plausible contributing factors. Together, these unresolved questions reveal the limitations of static, idealized models and point to the need to account for both the structural heterogeneity arising from synthesis and the dynamic nature of active sites under electrochemical conditions.

In this work, we develop a generalizable computational framework that connects catalyst synthesis and operation by integrating grand canonical DFT with machine-learning-accelerated sampling. Using NiN_xC_{4-x} (x = 0-4) as a model system —capturing coordination defects likely formed during high-temperature synthesis — we identify hydrogenated NiN_3C_1 as the most active configuration, offering an optimal balance of activity, selectivity, and stability behavior. Under reducing conditions, hydrogenation

occurs preferentially at C-Ni bridge sites, with subsurface hydrogen promoting the formation of bent CO_2 intermediates. CO_2RR selectivity is enhanced by two factors: spatial separation of active sites, with Ni centers facilitating CO_2RR and C-Ni bridge sites or N sites mediating HER, and thermodynamic suppression of HER under moderate hydrogen coverage. At more negative potentials, selectivity declines due to a shift in the RDP and potential-induced structural instabilities, including Ni detachment triggered by co-adsorption of H and H_2O. That this framework captures both the origin of high CO_2RR selectivity and its degradation under increasingly negative potentials demonstrates the necessity of modeling hydrogenated, dynamically evolving surfaces. This work provides molecular-level insights into how the environment, hydrogen coverage, and dynamic restructuring jointly govern catalytic performance, offering a general strategy for identifying true active sites under realistic reaction conditions.

Results

Thermodynamic Stability of Ni-N-C configurations under varying Hydrogen Coverage

Ni-N-C catalysts synthesized under high-temperature conditions can exhibit diverse coordination defects. To capture this structural diversity, we focus on a series of four-coordinated NiN_xC_{4-x} (x = 0-4) motifs embedded in graphene, which represent the most thermodynamically stable coordination environments for Ni single atom (**Figure S6**). Their stability was systematically evaluated under varying hydrogen coverages and reducing potentials, considering their function as cathodic active sites for CO_2 electroreduction. Our analysis reveals that hydrogen preferentially adsorbs at C-Ni bridge sites or N atoms rather than directly on the top of Ni center. For NiN_4, H adsorption is favored on the top of N (~0.5 eV more stable than on Ni), whereas for NiN_xC_{4-x} sites($x \neq 4$), the C-Ni bridge site is preferred over the N atoms by ~0.5 eV. To rationalize this preferential adsorption, we found the H adsorption energy to be influenced primarily by three factors: (i) the intrinsic H-X (X = C or N) binding strength, (ii) local structural distortions near the adsorption site upon H binding, and (iii) the

perturbation of Ni coordination environment (**Figures 1a-1c**). Nitrogen, with its lone pair, stabilizes the Ni center via strong dative interactions with Ni *d* orbitals.[8] While the N-H bonds are intrinsically stronger, shorter (1.07 Å) and associated with greater charge transfer (~0.5 e^-) than the C-H bonds (1.17 Å, ~0.1 e^-), their formation induces significant structural rearrangements. These include vertical displacement of the N atom, elongation of N-C bonds (from 1.35 Å to 1.43 Å), and weakening of the Ni-N interaction (from 1.95 Å to 2.01 Å). In contrast, H adsorption on C-Ni bridge site introduces minimal distortion and even slightly reinforces the Ni-N bonding (from 1.95 Å to 1.91 Å). Therefore, despite the nominally stronger N-H bond, the associated distortion of both the adsorption site and the Ni coordination environment renders C-Ni bridge site thermodynamically preferred.

Focusing on H adsorption at adjacent C and N sites, we evaluate H coverage effects, particularly their influence on Ni coordination and surface structural evolution. Notably, H adsorption is considered on both sides of the graphene plane, motivated by the possibility that protons may migrate through defects to the underside.[48] Indeed, the barrier for this migration is computed to be low (~ 0.4 eV at -1.0 V vs SHE, **Figure 1d** and **Figure S7**), with comparable adsorption energies for H on both sides of the plane. However, deeper intercalation of hydrogen into the bulk is energetically unlikely due to the high migration barrier in a defect-free lattice.[48] The most stable configurations at varying hydrogen coverages are identified in **Figures S8-S12**. As the applied potential becomes more negative, the H coverage increases correspondingly (**Figure 1e** and **Figure S13**). For instance, in the NiC_4 system, the bare surface is favored above 0.13 V, NiC_4H_2 dominates from 0.13 to -0.50 V, and NiC_4H_4 becomes most stable between -0.50 and -1.05 V. Beyond this, high-coverage configurations such as NiC_4H_8 emerge, accompanied by significant out-of-plane displacement of the Ni atom. Once six H atoms are adsorbed, the Ni center lifts significantly, indicating a critical threshold for structural destabilization (**Figure S8**). This voltage-dependent hydrogen coverage thus directly governs surface reconstruction. In comparison, the NiN_2C_2 motif exhibits stronger resistance to distortion, requiring much more negative potentials (~ -1.6 V) to induce similar Ni displacement, thereby reinforcing the stabilizing role of nitrogen

coordination (**Figure 1f**). At -1.0 V, the number of adsorbed H atoms typically matches the number of carbon neighbors around Ni (**Figure 1g**), and dual-side adsorption is found to be more stable than single-side configurations. In addition, stronger hydrogen binding is observed in systems with a higher number of adjacent carbon atoms at the same potential, underscoring the critical influence of local coordination on hydrogen adsorption thermodynamics (**Figure 1g**).

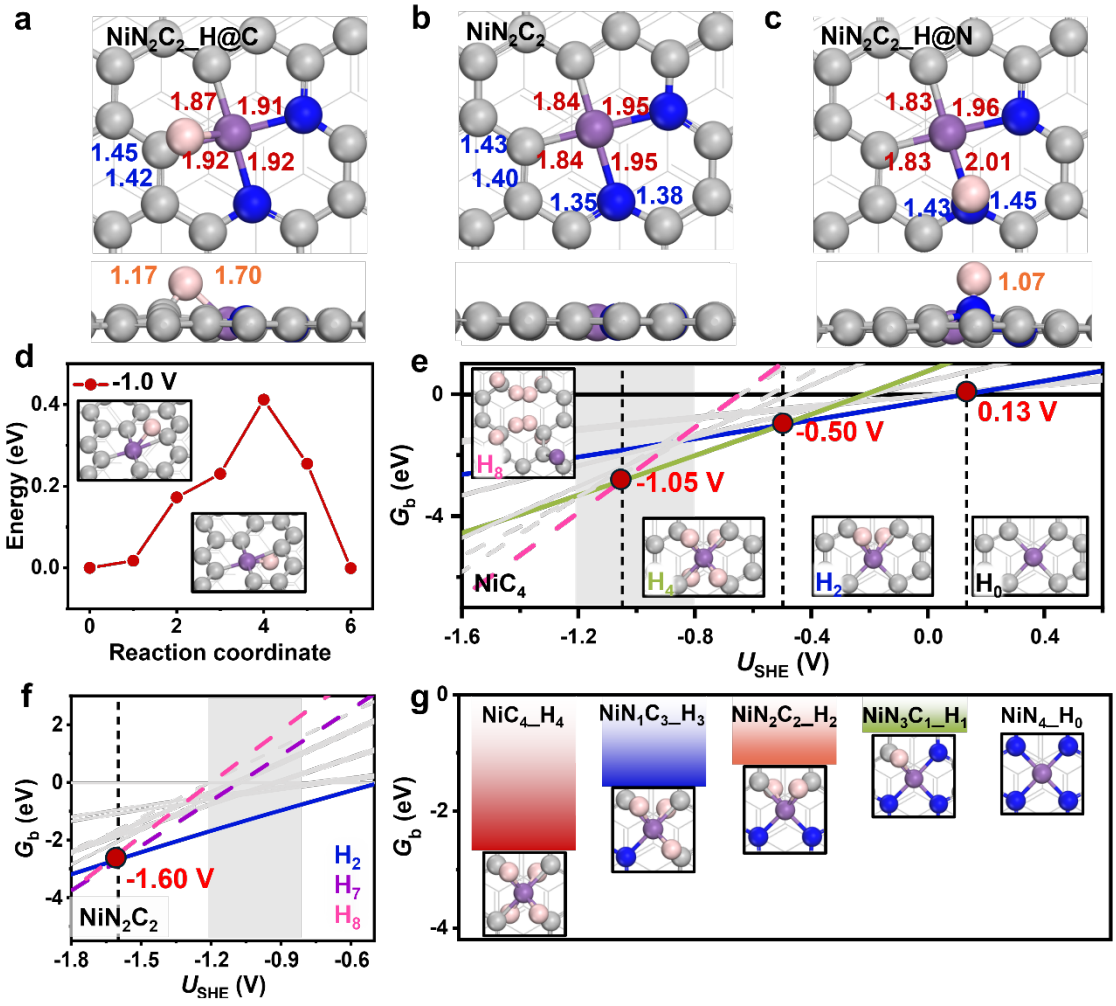

Figure 1. (a)-(c) Top and side views of the NiN_2C_2 configuration under different hydrogen adsorption scenarios: (a) H adsorbed on the C-Ni bridge site; (b) pristine (no H); (c) H adsorbed on the adjacent N atom. Bond lengths are given in Å. (d) Energy profile for H migration from the top to the bottom side of NiC_4 at -1.0 V vs SHE, with initial and final configurations shown. (e) Thermodynamic stability diagram of NiC_4 with varying hydrogen coverages as a function of applied potential. For each coverage, isomers within 0.2 eV of the global minimum at -1.0 V are considered. The lowest

surface energy structures are indicated by colored solid lines, while other configurations are shown in gray. More detailed assignments for each gray line are provided in the **Figure S13**. Dashed lines indicate the coverage at which Ni-leaching becomes thermodynamically favorable. Vertical black dashed lines denote the voltages at which the most stable configuration changes. Red circles indicate transition points with corresponding voltages and configurations indicated. The silver background highlights the experimentally relevant potential window for Ni-N-C catalysts (pH = 6.8). (f) Thermodynamic stability diagrams of NiN_2C_2 with different hydrogen coverages as a function of applied voltage. (g) Gibbs free energy of binding for the most stable hydrogen-covered configurations for different Ni-N-C motifs at -1.0 V vs SHE, with representative top views. Configurations involving Ni-leaching are excluded. Color code: purple, light gray, blue and pink represent Ni, C, N and surface-adsorbed H, respectively.

Impact of H coverage and distribution on CO_2RR and HER

Given the inherent chemical inertness of the linear O=C=O molecule, CO_2 adsorption and activation are widely regarded as key prerequisites for initiating CO_2RR.[45,49] To this end, we evaluated the influence of H coverage on CO_2 binding across different Ni-N-C configurations, considering both linear and bent adsorption configurations. The bent geometry is typically indicative of stronger metal-CO_2 interactions and partial activation of the molecule, which can facilitate subsequent proton-coupled electron transfer (PCET) steps. On the bare surface, we observed that increasing the number of coordinated carbon atoms enhances the CO_2 binding strength (**Figure S14**). This trend correlates well with Bader charge analysis (**Figure 2a**), which shows that higher degree of carbon coordination leads to a higher electron density on the Ni center (i.e., less positive charge), thereby strengthening CO_2 adsorption. Among all studied motifs, CO_2 adsorption is thermodynamically feasible for all except the NiN_4 configuration.

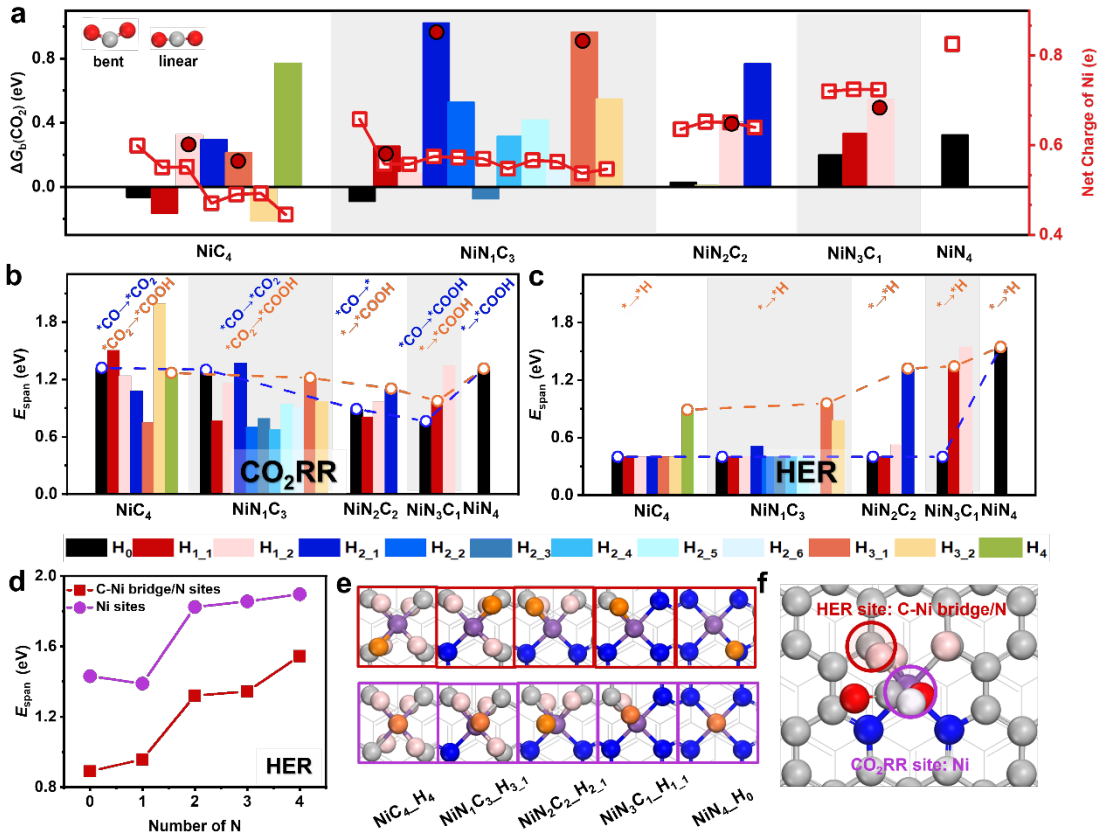

Figure 2. (a) Gibbs free energy differences between bent and linear CO_2 adsorption geometries ($\Delta G_b(CO_2) = G_{bent} - G_{linear}$) at -1.0 V vs SHE for different Ni-N-C motifs with varying hydrogen coverages (bars, left y-axis). Red hollow circles (right y-axis) represent the net Bader charge of Ni atoms in the corresponding structures without CO_2 adsorption. Red-filled circles highlight isomers that, within the same NiN_xC_{4-x} composition and hydrogen coverage(H_{n_m}) , possess the largest number of H atoms adsorbed above the graphene plane. H_{n_m} indicates the number (n) of adsorbed hydrogen atoms and the isomer index (m) at a given coverage, shown at the bottom of the figure b. (b-c) Energy span (E_{span}) analysis for CO_2RR and HER at -1.0 V vs SHE across Ni-N-C motifs. Blue dashed lines represent the change of E_{span} on the bare surface, while orange dashed lines correspond to the most thermodynamically stable hydrogen-covered configurations at -1.0 V. The associated RDP is annotated above each bar in the corresponding color (blue for bare, orange for hydrogen-covered). (d) Comparison of E_{span} values for HER on C-Ni bridge/N sites versus Ni sites on the

most thermodynamically stable hydrogen-covered configurations of Ni-N-C at -1 V. (e) Top-view structures corresponding to the HER configurations analyzed in (d), with hydrogen adsorption sites highlighted in orange. (f) Schematic illustration of spatially separated active sites on Ni-N-C motifs: CO_2 reduction occurs on the top of Ni center, while hydrogen evolution takes place at C-Ni bridge site or N site. Color code: white indicates H in intermediates (e.g., H_2O, *COOH), not directly adsorbed on the surface.

When surface hydrogenation is considered, specifically, the most thermodynamically stable hydrogen-covered configurations for Ni-N-C composition at -1.0 V vs SHE, CO_2 binding is generally weakened compared to the corresponding bare surfaces (**Figure S14**). Among them, $NiN_1C_3\_H_3$ shows the strongest binding, followed by $NiC_4\_H_4$ > $NiN_2C_2\_H_2$ > $NiN_3C_1\_H_1$ > $NiN_4\_H_0$, a trend that largely correlates with Bader charge, except NiC_4H_4. When thermodynamic stability is disregarded and CO_2 binding is examined solely as a function of H coverage, non-monotonic trends emerge: in some cases, increasing hydrogen coverage strengthens CO_2 binding, while in others it weakens. This behavior arises from differences in the spatial arrangement of adsorbed hydrogen. Notably, even at the same H coverage, variations in the H adsorption configuration significantly affect CO_2 activation, as reflected by the energy difference between bent and linear CO_2 adsorption. Isomers with the largest number of H atoms adsorbed above the graphene plane (denoted by red-filled circle in **Figure 2a**) exhibit more positive energy differences between the bent and linear CO_2 adsorbed structures, indicating less favorable CO_2 bending; in contrast, bottom-side hydrogen adsorption facilitates CO_2 bending and thus activation. Although Bader charge analysis reveals only small variation in the electronic properties of Ni centers across these isomers (**Figure 2a**), the steric environment induced by the specific H adsorption geometry plays a key role in modulating CO_2 activation. In summary, increasing the number of coordinated carbon atoms consistently strengthens CO_2 adsorption, both with and without hydrogen coverage. However, hydrogen adsorption generally weakens CO_2 binding, and configurations with hydrogen adsorbed below the graphene plane are more favorable for CO_2 activation due to reduced steric hindrance.

We then modeled the full CO_2RR and HER pathways under different H coverages using the energy span(ES) model,[50–52] where catalytic activity is determined by the largest energy gap between the turnover-frequency (TOF) determining transition state and intermediate, termed as the rate-determining process (RDP) at -1 V vs SHE. . The idea of defining catalytic activity via the RDP, instead of a single rate-limiting step, is consistent with the degree of rate control framework commonly used in microkinetic modeling.[53] All thermodynamic data used as inputs to the ES model are obtained from GC-DFT calculations. Details of the reaction mechanism and ES model are provided in the Supporting Information(SI). In the absence of hydrogen coverage (i.e., on the bare surface), for CO_2RR, NiN_3C_1 exhibits the highest activity, followed by NiN_2C_2 while the remaining configurations show similarly low catalytic performance (**Figure 2b**). In these cases, the RDP is *CO desorption, except for NiN_4, where the formation of *COOH is rate-limiting. [22] For HER, all configurations except NiN_4 show comparable activity, with NiN_4 being markedly less favorable (**Figure 2c**). For NiN_4, *H adsorption (Volmer step) is RDP, whereas for others, both *H adsorption and *H desorption (Heyrovsky step) contribute comparably to the ES(**Figure S15**). Overall, HER is thermodynamically more favorable (0.40 eV) than CO_2RR (0.76-1.32 eV) for $NiN_xC_{4-x}(x \neq 4)$. For NiN_4, HER is slightly less favorable than CO_2RR (1.54 vs 1.31 eV), suggesting good selectivity but low activity towards CO_2RR. This is consistent with prior reports,[37] failing to explain the origin of the high CO_2RR activity and selectivity of Ni-N-C catalysts.

When considering the most stable hydrogen-covered structures at -1.0 V, we observe that for CO_2RR, the activity of NiC_4 and NiN_1C_3 slightly improves, while that of NiN_2C_2 and NiN_3C_1 slightly declines. The overall trend closely resembles that of the bare surface. Notably, for all structures, the RDP shifts to the *COOH formation, aligning well with experimental observations (**Figure 2b**).[35] For HER, however, hydrogen coverage significantly suppresses catalytic activity across all structures, as reflected by the increased E_{span} values (0.49-0.94 eV), along with a universal shift of the RDP to *H adsorption (**Figure 2c**). This suppression arises from the saturation of

carbon coordination (reaching four) on hydrogenated surfaces, making further H adsorption at C-Ni bridge sites thermodynamically unfavorable. H adsorption on Ni sites becomes even less favorable, resulting in an additional increase in E_{span} by 0.35-0.54 eV compared to adsorption at C-Ni bridge or N sites (**Figures 2d** and **2e**). These results confirm that HER still occurs at C-Ni bridge or N sites when surface hydrogenation is taken into account. [54] , challenging the common perception that HER occurs at the metal site.[55] Therefore, both the suppression of HER under moderate hydrogen coverage and the spatial separation of active sites contribute synergistically to the high CO_2RR selectivity of Ni-N-C catalysts(**Figure 2f**). Moreover, our findings highlight a critical limitation in current HER catalyst screening strategies, which often assess hydrogen adsorption only on metal centers.[56,57] Such an approach neglects the influence of surrounding heteroatoms and surface hydrogenation, potentially leading to misleading predictions of catalytic performance.

Potential-Dependent Evolution of Activity and Selectivity in Ni−N−C configurations

To systematically evaluate how catalytic activity evolves with applied potential, we first analyzed the Boltzmann population(p_i) of different hydrogen-covered isomers across different potentials using **Equation 2** (**Figure 3a** and **Figure S16**). Taking NiN_1C_3 as a representative case, the isomers $NiN_1C_3\_H_{3\_1}$ and $NiN_1C_3\_H_{3\_2}$ dominate the ensemble across the potential range studied, with comparable populations. As the potential becomes more negative, the population of $NiN_1C_3\_H_{3\_1}$ gradually decreases, while that of $NiN_1C_3\_H_{3\_2}$ increases. Then we evaluate the E_{span} for each isomer under different potentials for both CO_2RR (**Figure 3b** and **Figure S17**) and HER (**Figure 3c** and **Figure S18**), with the corresponding RDP summarized in **Tables S1** and **S2**. For CO_2RR, E_{span} exhibits diverse trends: in many cases, it decreases with decreasing potential. However, in some cases, it first decreases then increases due to a potential-induced shift in the RDP. In a few cases, it remains relatively unchanged. In contrast, for HER, E_{span} generally decreases monotonically as the potential becomes more

negative.

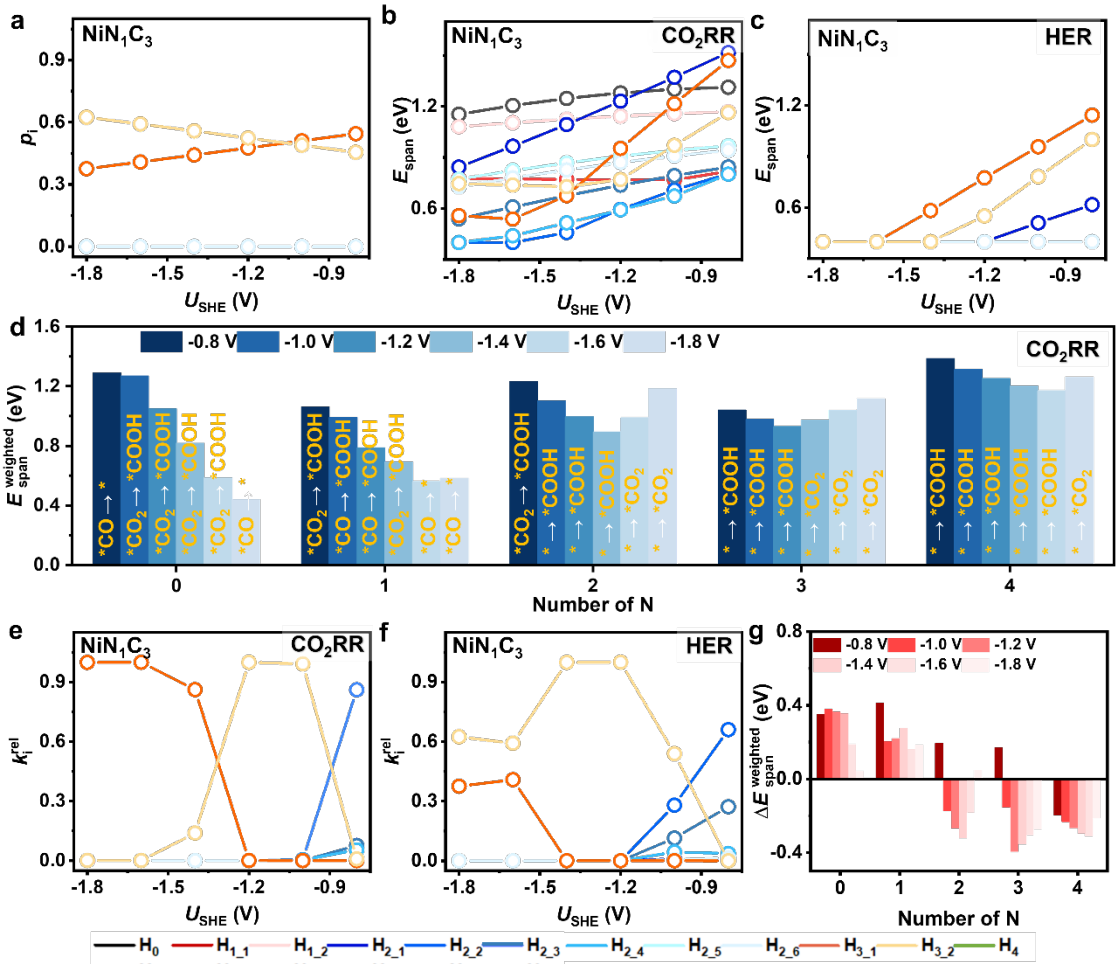

Figure 3. (a) Boltzmann population(p_i) of different hydrogen-covered isomers of NiN_1C_3 as a function of applied potential. Each colored line represents a specific H-covered configuration, with labels shown at the bottom of the figure. (b-c) E_{span} values for CO_2RR (b) and HER (c) across various H-covered NiN_1C_3 isomers under different applied potentials. (d) Boltzmann-weighted energy spans ($E_{span}^{weighted}$) for CO_2RR at different applied potentials across different Ni-N-C motifs. The x-axis denotes the number of coordinated N atoms. Yellow labels indicate the corresponding RDP for each case (e-f) Relative contributions of different hydrogen-covered isomers to the overall CO_2RR(e) and HER (f) for NiN_1C_3 at various potentials. (g) Difference in $E_{span}^{weighted}$ between CO_2RR and HER across the Ni-N-C motif under various applied potentials. More negative values signify higher CO_2RR selectivity.

To account for the ensemble-averaged catalytic behavior of all accessible configurations, we then evaluated the Boltzmann-weighted energy span ($E_{\mathrm{span}}^{\mathrm{weighted}}$, **Equation 4**) across the ensemble for each Ni-N-C catalysts (**Figure 3d**) by combining their Boltzmann-weighted populations with the corresponding E_{span}. Within the experimentally relevant potential range (-0.8 to -1.2 V), the activity trend follows: $NiN_3C_1 \approx NiN_1C_3 > NiN_2C_2 > NiC_4 > NiN_4$. While the activity of NiC_4 increases monotonically with more negative potential, others exhibit a volcano-type behavior, which is consistent with experimentally observed activity trends.[34] For HER, the trend is: $NiN_1C_3 > NiC_4 > NiN_2C_2 \approx NiN_3C_1 > NiN_4$, with most catalysts (except NiN_3C_1) showing enhanced HER activity under more negative potentials (**Figure S19**).

To further resolve the origin of these activity trends, we analyzed the potential-dependent relative reaction contributions of individual isomers for different reactions(k_i^{rel}, **Equation 5**), from which we can know which configurations dominate the catalytic ensemble at a given potential. For CO_2RR on NiC_4, as the potential becomes more negative, the contribution of the dominant species at -0.8V($NiC_4\_H_{3\_1}$) decreases, while that of $NiC_4\_H_4$ increases, overtaking $NiC_4\_H_{3\_1}$, around -1.0 V and dominating the active ensemble from -1.0 V to -1.8 V(**Figure S19a**) . For NiN_1C_3, the dominant active configuration also shifts with potential: $NiN_1C_3\_H_{2\_2}$ dominates the active ensemble at -0.8V. As the potential becomes more negative, $NiN_1C_3\_H_{3\_2}$ governs activity from -1.0 to -1.3 V, while $NiN_1C_3\_H_{3\_1}$ becomes dominant at more negative potential (**Figure 3e**). Although both isomers have similar Boltzmann populations, $NiN_1C_3\_H_{3\_2}$ initially has a lower E_{span} (0.97 vs 1.22 eV at -1 V), which increases at more negative potentials due to a shift in the RDP from *CO → *COOH to *CO →*. For other catalysts, $NiN_2C_2\_H_2$, $NiN_3C_1\_H_{1\_1}$, and NiN_4 remain the primary contributors to CO_2RR over the considered potential range **(Figure S20**). The RDPs of the dominant species for each Ni–N–C configuration at different potentials are indicated in **Figure 3d.** The volcano-like activity trends are governed by RDP

crossovers: while NiN_2C_2, NiN_3C_1 and NiN_4 exhibit a shift from *COOH formation to $*CO_2$ adsorption, NiN_1C_3 shifts from *COOH formation to *CO desorption. For HER, a similar analysis was conducted to assess the relative contributions of different isomers (**Figure 3f** and **Figure S21**). At -0.8 V, $NiN_1C_3\_H2\_2$ and $NiN_1C_3\_H2\_3$ contribute significantly to HER due to their low barriers, despite low populations. As the potential becomes more negative, $NiN_1C_3\_H3\_1$ and $NiN_1C_3\_H3\_2$ emerge as the dominant active species. Interestingly, the most active isomers differ between CO_2RR and HER within the same Ni-N-C system at potentials below -1.3 V (**Figures 3e-f**), emphasizing the necessity of evaluating reaction-specific ensemble contributions. The dominant active species can change with potential, driven either by changes in Boltzmann populations or variations in intrinsic activity. These findings underscore the importance of including low-energy ensemble of metastable states when assessing catalytic activity.[58–60]

To assess the selectivity for CO_2RR vs. HER, we used the difference in $E_{\text{span}}^{\text{weighted}}$ between these two reactions as a descriptor — a more negative value of this indicates higher CO_2RR selectivity (**Figure 3g**). NiC_4 and NiC_3N_1 exhibit poor CO_2RR selectivity, while NiN_4, NiN_3C_1 and NiN_1C_3 show superior selectivity. For these three, selectivity first increases and then decreases with potential, closely mirroring experimental observations.[34,35] When considering both activity and selectivity, NiN_3C_1 and NiN_2C_2 emerges as the most promising catalyst, followed by NiN_4.

For comparison, the bare-surface configurations were also evaluated with the change of potential (**Fig. S22**). Compared to the hydrogenated surface, bare structures show slightly improved CO_2RR activity but substantially enhanced HER activity. Among them, only NiN_4 reproduces the potential-dependent selectivity reversal observed experimentally, albeit with low CO_2RR activity (1.31 eV at -1 V). All other bare-surface configurations fail to reproduce the observed selectivity trends. This inability to reproduce potential-dependent selectivity in the absence of surface hydrogenation further highlights the importance of accounting for hydrogen coverage for an accurate description of the catalyst structure and activity under realistic operating conditions.

Potential-Dependent Stability of Ni−N−C Configurations under Co-adsorption of H and H_2O

Beyond activity and selectivity, the stability of SACs under working conditions remains a critical yet underexplored issue in electrocatalysis. While significant efforts have been devoted to understanding structure-activity relationships, the corresponding structure-stability relationships are less well established. [46,61] Here, we observed that increasing the number of coordinated hydrogen atoms progressively weakens the anchoring of the Ni atom, promoting its detachment from the surface. Previous reports have suggested that such detachment is more likely under co-adsorption conditions involving multiple adsorbates such as CO, OH, or H_2O in addition to hydrogen, which collectively destabilize the metal center.[29,30,62] Motivated by this, we systematically investigated the co-adsorption of H and H_2O to simulate pre-reaction surface environment, enumerating all plausible adsorption configurations involving 0-4 H_2O molecules and 0-8 H atoms on representative Ni-N-C structures (**Figure 4a**). We must admit that under realistic reaction conditions, strongly binding reaction intermediates (e.g., *COOH, *CO) are likely present and may further destabilize the metal center more effectively than H_2O, thus amplifying the leaching tendency.

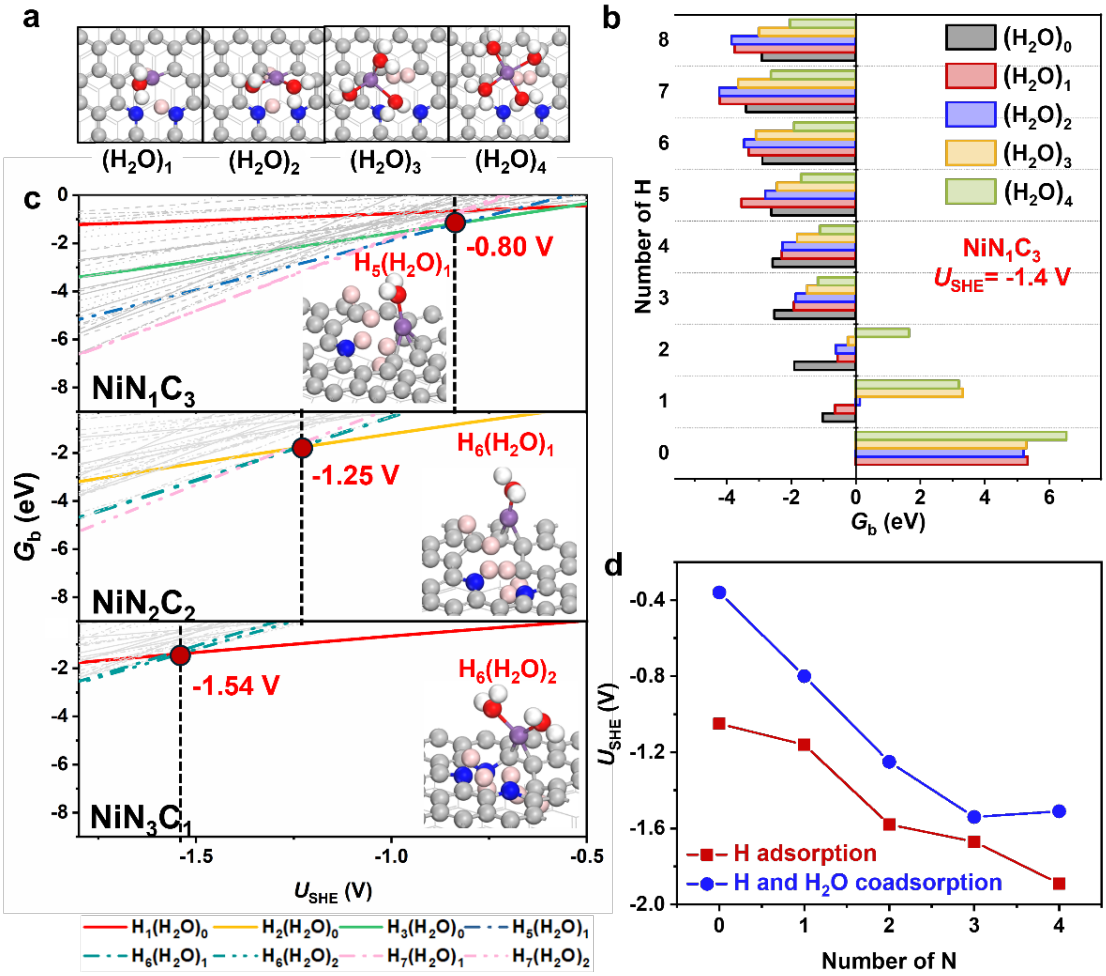

Figure 4. (a) Top views of NiN_2C_2_H_2 configurations with varying numbers of adsorbed water molecules: $1H_2O$, $2H_2O$, $3H_2O$, and $4H_2O$. (b) Gibbs free energy of binding energy of H and H_2O on the NiN_1C_3 under U_{SHE} = -1.4 V (c) Thermodynamic stability diagrams of various H/H_2O co-adsorbed configurations on NiN_1C_3, NiN_2C_2, and NiN_3C_1 as a function of applied potential. The lowest surface energy structures are indicated by colored solid lines, while other configurations are shown in gray. More detailed assignments for each gray line are provided in the **Figures S23-27**. Vertical black dashed black lines mark critical voltages where the Ni atom transitions from an in-plane to an out-of-plane (detachment) configuration, with numerical values indicated. Insets show representative structures of the detachment configurations. (d) Onset voltages for Ni detachment from the surface as a function of the number of coordinated nitrogen atoms, under conditions of H-only adsorption versus H/H_2O co-adsorption.

Because the configuration space is too vast for exhaustive DFT sampling, we developed a machine learning potential (MLP) based on the Recursively Embedded Atom Neural Network (REANN)[63], trained for this system to accelerate exploration. The model achieves a root mean square error (RMSE) of 0.003 eV/atom for energy predictions and force RMSEs of 0.05 eV/Å (C, H), 0.08 eV/Å (N), 0.07 eV/Å (O), and 0.12 eV/Å (Ni), demonstrating high accuracy and robust performance in capturing the structural complexity of SACs systems. Further details are provided in the SI. From the MLP-optimized database, the 200 lowest-energy configurations for each Ni-N-C motif at a given H/H_2O coverage were selected for further DFT refinement, forming the basis for global minimum (GM) structure identification. Interestingly, the Ni atom remains embedded within the coordination plane in the absence of H adsorption (i.e., only H_2O is present), as the G_b remain positive (**Figure 4b** and **Figure S28**), highlighting that hydrogen adsorption is the primary factor governing the stability of Ni single-atom sites. Our results reveal that Ni preferentially coordinates with up to two H_2O molecules, whereas binding three or four H_2O molecules is energetically unfavorable. In addition, Upon H_2O coordination, the relatively large volume of the water molecules and a decrease in the Ni coordination number with surface C/N atoms (to 0~3) weaken the anchoring, thereby driving the Ni atom to protrude from the graphene plane and detach from the substrate (**Figure 4c**). In our model, detachment is defined as the vertical displacement of the Ni atom beyond the graphene plane ($\Delta z > 1.0$Å), which represents a structural precursor to instability and potential aggregation that may ultimately result in cluster formation. As the number of coordinated N atoms increases from 1 to 3, the critical potential for Ni detachment shifts from -0.80 V to -1.25 V and -1.54 V, indicating enhanced stability with increasing N coordination. We further compared critical detachment potentials under two scenarios: only H adsorption, and co-adsorption of H and H_2O (**Figure 4d**). The results clearly show that co-adsorption leads to a more positive critical potential, making Ni detachment thermodynamically more favorable. This highlights the necessity of considering not only hydrogen but also co-adsorbates when evaluating the stability of single-atom catalysts under realistic electrochemical conditions.

These findings suggest that the experimentally observed decline in CO_2RR selectivity at more negative potentials may partially arise from the potential-induced detachment of Ni atoms. Together, both the potential-dependent shift in the rate-determining process and the destabilization of Ni SACs contribute to the overall loss of CO_2RR activity and selectivity. Considering activity, selectivity, and stability, the $NiN_3C_1\_H_1$ configuration emerges as the most promising active site across all Ni-N-C motifs under operating conditions. From an electronic structure perspective, the Ni atom in NiN_4 is in the Ni^{2+} oxidation state, whereas Ni in $NiN_3C_1\_H_1$ exhibits a lower oxidation state (**Figure 2a**), showing a tendency toward Ni^{1+}. This lends some support to experimental findings that Ni^{1+} is the true catalytically active species under working conditions. [35,38,39,42]

Conclusion

In this work, we have combined grand canonical DFT calculations with machine-learning-accelerated potential energy surface sampling to uncover the dynamic structure-activity-stability relationships governing Ni-N-C single-atom catalysts under electrochemical CO_2 reduction conditions. Our results demonstrate that under reducing electrode potential, spontaneous hydrogenation of the surface occurs preferentially at C-Ni bridge sites, with subsurface hydrogen playing a key role in stabilizing catalytically relevant bent CO_2 intermediates. We show that CO_2RR selectivity arises from (1) spatial separation of active sites to enable functional differentiation between CO_2RR and HER and (2) suppression of HER at moderate hydrogen coverage. However, at more negative potential, this selectivity deteriorates due to a shift in the RDP for CO_2RR and the onset of structural instabilities including Ni detachment induced by co-adsorption of H and H_2O. By systematically evaluating activity, selectivity, and stability, we identify $NiN_3C_1\_H_1$ as the most robust and active configuration under operating conditions. Importantly, the inclusion of hydrogen coverage in our modeling enables rationalization of two key experimental observations: the high intrinsic selectivity of Ni-N-C catalysts and the potential-dependent reversal

in CO_2RR selectivity. These findings emphasize the need to move beyond static models and explicitly account for coordination environment, hydrogenation states, and potential-induced structural evolution when designing next-generation single-atom catalysts. Additional environmental factors beyond the intrinsic active site configuration, such as pH, cations, anions, and explicit solvation may also modulate interfacial reactivity and remain an important direction for future investigation.

Methods

DFT calculations

All plane-wave density functional theory (DFT) calculations were carried out using the Vienna Ab Initio Simulation Package (VASP)[64,65] with the Perdew-Burke-Ernzerhof (PBE) exchange-correlation functional within the generalized gradient approximation (GGA) framework.[66] The projector-augmented-wave (PAW) method was employed with a kinetic energy cutoff of 400 eV. Model systems were constructed using a p(5 × 5) surface unit cell comprising three atomic layers. The bottom two layers were fixed to mimic the bulk environment, while the top layer and all adsorbates were fully relaxed to represent the interfacial structure. A vacuum region of 20 Å was applied along the z-direction to avoid spurious interactions between periodic images. For simulations involving implicit solvation and surface charging, all structures were symmetrized, and the simulation cell was extended to 60 Å in the z-direction to accommodate the implicit solvent region. Geometry optimizations were performed until forces on all relaxed atoms were below 0.05 eV/Å, with an energy convergence threshold of 10^{-5}eV. A Γ-point-only (1 × 1 × 1) k-point mesh was used for all structural relaxations. Gibbs free energies of adsorbed species were computed by correcting the DFT total energies with zero-point energy (ZPE) and entropy contributions, obtained from vibrational frequency analyses within the harmonic oscillator approximation. Grand canonical free energies were evaluated using grand canonical density functional theory (GC-DFT), a surface-charging-based approach. Further details on the GC-DFT methodology are provided in the Supporting Information and in our previous work.[67–69] All

electrochemical data were analyzed within the GC-DFT framework.

Machine-learning atomic simulation

Due to the high computational cost associated with DFT calculations, which limits the scale and diversity of accessible configurational sampling, we developed a machine-learning (ML) potential to accelerate structural optimization and expand the explored configurational space. Specifically, we constructed a neural network (NN) potential for the Ni-C-N-O-H quinary system using the recursively embedded atom neural network (REANN) framework,[63] which employs a 5.0 Å neighbor cutoff, eight primitive Gaussian-type orbitals, an atomic energy fitting network of 128×128, and three message-passing loops, each using a 64×64 fitting net. This model demonstrates high accuracy and reliability in predicting structural energetics of complex catalytic systems (**Figure S4**).

To generate the configurational dataset, we first sampled Ni adsorption sites near C/N defects on Ni-free N-C surfaces, systematically covering Ni coordination numbers from 1 to 4. Approximately 385 representative Ni-N-C motifs were constructed and filtered by structural similarity. For each motif, we enumerated 255 hydrogen adsorption configurations corresponding to all possible combinations of 1-8 H atoms distributed over adjacent C/N site from both sides. These hydrogenated motifs were then systematically combined with $Ni(H_2O)_n$ clusters (n = 0-4), replacing the original Ni site, and rotational variants of the water molecules were introduced to capture orientational flexibility. This procedure yielded over hundreds of thousands of distinct configurations for each Ni-N-C motif. Training data were collected from these structures and their optimization trajectories using an active learning strategy. Structures were iteratively selected based on uncertainty model (thresholds of 0.05-0.25 eV/atom) and CUR decomposition sampling.[70–74] The computational workflow utilizes an open-source package called "Generating Deep Potential with Python (GDPy)" for implementing these advanced models.[75] The final dataset comprises 230 chemically distinct systems and 38,042 total configurations. After identifying low-energy

candidates through the NN, high-fidelity DFT calculations were performed to validate the most thermodynamically stable structures for subsequent analysis.

Atomistic thermodynamics

To assess catalytic reactivity across different hydrogen coverages, we employed the energy span (ES) model proposed by Kozuch and Shaik,[50,51] which approximates the reaction rate by the largest free energy difference between a transition state and an intermediate along the catalytic cycle. In our system, all elementary steps involve proton-coupled electron transfer (PCET), which are known to exhibit similar barrier profiles. To reduce computational cost, we assumed a uniform free energy barrier of 0.4 eV for all steps, consistent with prior studies.[76]

The thermodynamic stability of each structure was evaluated by calculating the binding free energy (G_{b}) of co-adsorbed hydrogen and water molecules Ni-N-C plane, defined as follows:

$$G_{\mathrm{b}} = G_{\mathrm{Ni-N-C+nH+mH2O}} - G_{\mathrm{Ni-N-C}} - \mathrm{n}\mu_{\mathrm{H}} - \mathrm{m}G_{\mathrm{H2O}} \quad (1)$$

where $G_{\mathrm{Ni-N-C+nH+mH2O}}$ is the total Gibbs free energy of the composite system and μ_{H} and G_{H2O} are reference free energies for hydrogen and water, respectively.

The Boltzmann population p_i of each structure i was computed based on its G_{b} as:[58,59,77–79]

$$p_i = \mathrm{e}_i^{-\beta \triangle G_b^i} / \sum_{j \epsilon S} \mathrm{e}^{-\beta \triangle G_b^j} \quad (2)$$

where β is $1/k_{\mathrm{B}}T$, k_{B} is the Boltzmann constant, T is the temperature (set to 298.15 K) and S denotes the ensemble of all thermodynamically accessible structures.

To assess the catalytic contribution of each configuration, we used the weighted reaction rate k_i^w, which combines stability based on the structure population p_i and activity described by the Arrhenius equation

$$k_i^w = A \cdot e^{-\beta E_{span}^i} \cdot p_i \quad (3)$$

where A represents the rate constant of any reaction and E_{span}^i represents the energy span of configuration i. We assume that the rate constant of the same reaction remains constant. The specific value of A is not considered, as our aim is to evaluate the relative reactivity of each structure.

A single kinetic descriptor that captures the activity of the full ensemble, the Boltzmann-weighted energy span, was defined as:

$$E_{\text{span}}^{\text{weighted}} = -k_B T \sum_{j \epsilon S} k_j^w) \quad (4)$$

Finally, the relative reaction contribution of the i-th structure is defined as:

$$k_i^{\text{rel}} = k_i^w / \sum_{j \epsilon S} k_j^w \quad (5)$$

where the nominator is the summation of the weighted reaction rate of S-reactive structures.

Supporting Information available:

Computational details, machine learning potential development, thermodynamic stability data, impact of H coverage on reactivity, potential-dependent evolution of stability, activity, and selectivity of the Ni-N-C sites.

Acknowledgements

This work was supported as part of the Center for Closing the Carbon Cycle, an Energy Frontier Research Center funded by the U.S. Department of Energy, Office of Science, Basic Energy Sciences under Award Number DE-SC0023427. Our calculations utilized resources of Perlmutter of the National Energy Research Scientific Computing Center (NERSC) under Contract DE-AC02-05CH11231. The authors gratefully acknowledge Shawn Chiu, Dr Ke Ye and Dr. Jiayan Xu for fruitful discussions.

References

(1) Wang, A.; Li, J.; Zhang, T. Heterogeneous Single-Atom Catalysis. *Nat. Rev. Chem.* **2018**, *2* (6), 65–81.

(2) Yang, X.-F.; Wang, A.; Qiao, B.; Li, J.; Liu, J.; Zhang, T. Single-Atom Catalysts: A New Frontier in Heterogeneous Catalysis. *Acc. Chem. Res.* **2013**, *46* (8), 1740–1748.

(3) Fu, Q.; Saltsburg, H.; Flytzani-Stephanopoulos, M. Active Nonmetallic Au and Pt Species on Ceria-Based Water-Gas Shift Catalysts. *Science* **2003**, *301* (5635), 935–938.

(4) Hannagan, R. T.; Giannakakis, G.; Flytzani-Stephanopoulos, M.; Sykes, E. C. H. Single-Atom Alloy Catalysis. *Chem. Rev.* **2020**, *120* (21), 12044–12088.
(5) Vijay, S.; Ju, W.; Brückner, S.; Tsang, S.-C.; Strasser, P.; Chan, K. Unified Mechanistic Understanding of CO_2 Reduction to CO on Transition Metal and Single Atom Catalysts. *Nat.Catal.* **2021**, *4* (12), 1024–1031.
(6) Thomas, J. M.; Raja, R.; Lewis, D. W. Single-Site Heterogeneous Catalysts. *Angew. Chem. Int. Ed.* **2005**, *44* (40), 6456–6482.
(7) Cui, Y.; Ren, C.; Wu, M.; Chen, Y.; Li, Q.; Ling, C.; Wang, J. Structure–Stability Relation of Single-Atom Catalysts under Operating Conditions of CO_2 Reduction. *J. Am. Chem. Soc.* **2024**, *146* (42), 29169–29176.
(8) Cui, Y.; Ren, C.; Li, Q.; Ling, C.; Wang, J. Hybridization State Transition under Working Conditions: Activity Origin of Single-Atom Catalysts. *J. Am. Chem. Soc.* **2024**, *146* (22), 15640–15647.
(9) Lei, J.; Zhu, T. Impact of Potential and Active-Site Environment on Single-Iron-Atom-Catalyzed Electrochemical CO_2 Reduction from Accurate Quantum Many-Body Simulations. *ACS Catal.* **2024**, *14* (6), 3933–3942.
(10) Ou, Y.; Liu, L.; Seemakurthi, R. R.; You, F.; Ma, H.; Pérez-Ramírez, J.; López, N.; Yeo, B. S. Controlling Hydrocarbon Chain Growth and Degree of Branching in CO2 Electroreduction on Fluorine-Doped Nickel Catalysts. *Nat.Catal.* **2025**, 1–14.
(11) Martini, A.; Hursán, D.; Timoshenko, J.; Rüscher, M.; Haase, F.; Rettenmaier, C.; Ortega, E.; Etxebarria, A.; Roldan Cuenya, B. Tracking the Evolution of Single-Atom Catalysts for the CO_2 Electrocatalytic Reduction Using Operando X-Ray Absorption Spectroscopy and Machine Learning. *J. Am. Chem. Soc.* **2023**, *145* (31), 17351–17366.
(12) Ju, W.; Bagger, A.; Hao, G.-P.; Varela, A. S.; Sinev, I.; Bon, V.; Roldan Cuenya, B.; Kaskel, S.; Rossmeisl, J.; Strasser, P. Understanding Activity and Selectivity of Metal-Nitrogen-Doped Carbon Catalysts for Electrochemical Reduction of CO2. *Nat. Commun.* **2017**, *8* (1), 1–9.
(13) Han, Y.; Li, Q.-K.; Ye, K.; Luo, Y.; Jiang, J.; Zhang, G. Impact of Active Site Density on Oxygen Reduction Reactions Using Monodispersed Fe–N–C Single-Atom Catalysts. *ACS Appl. Mater. Interfaces* **2020**, *12* (13), 15271–15278.
(14) Han, Y.; Ye, K.; Huang, Y.; Wu, Z.; Hu, P.; Zhang, G. Leveraging Interlayer Interaction in M–N–C Catalysts for Enhanced Activity in Oxygen Reduction Reactions. *J. Phys. Chem. Lett.* **2023**, *14* (44), 9900–9908.
(15) Zhang, D.; Wang, Z.; Liu, F.; Yi, P.; Peng, L.; Chen, Y.; Wei, L.; Li, H. Unraveling the pH-Dependent Oxygen Reduction Performance on Single-Atom Catalysts: From Single- to Dual-Sabatier Optima. *J. Am. Chem. Soc.* **2024**, *146* (5), 3210–3219.
(16) Kim, K.; Kim, G.; Jeong, T.; Lee, W.; Yang, Y.; Kim, B.-H.; Kim, B.; Lee, B.; Kang, J.; Kim, M. Activating the Mn Single Atomic Center for an Efficient Actual Active Site of the Oxygen Reduction Reaction by Spin-State Regulation. *J. Am. Chem. Soc.* **2024**, *146* (49), 34033–34042.
(17) Di Liberto, G.; Cipriano, L. A.; Pacchioni, G. Role of Dihydride and Dihydrogen

Complexes in Hydrogen Evolution Reaction on Single-Atom Catalysts. *J. Am. Chem. Soc.* **2021**, *143* (48), 20431–20441.

(18) Ye, S.; Liu, F.; She, F.; Chen, J.; Zhang, D.; Kumatani, A.; Shiku, H.; Wei, L.; Li, H. Hydrogen Binding Energy Is Insufficient for Describing Hydrogen Evolution on Single-Atom Catalysts. *Angew. Chem. Int. Ed.* **2025**, *137* (23), e202425402.

(19) Liu, X.; Zheng, L.; Han, C.; Zong, H.; Yang, G.; Lin, S.; Kumar, A.; Jadhav, A. R.; Tran, N. Q.; Hwang, Y.; Lee, J.; Vasimalla, S.; Chen, Z.; Kim, S.-G.; Lee, H. Identifying the Activity Origin of a Cobalt Single-Atom Catalyst for Hydrogen Evolution Using Supervised Learning. *Adv. Funct. Mater.* **2021**, *31* (18), 2100547. h

(20) Zhang, Z.; Xiao, J.; Chen, X.-J.; Yu, S.; Yu, L.; Si, R.; Wang, Y.; Wang, S.; Meng, X.; Wang, Y.; Tian, Z.-Q.; Deng, D. Reaction Mechanisms of Well-Defined Metal–N4 Sites in Electrocatalytic CO_2 Reduction. *Angew. Chem. Int. Ed.* **2018**, *57* (50), 16339–16342.

(21) Wang, Z.-L.; Choi, J.; Xu, M.; Hao, X.; Zhang, H.; Jiang, Z.; Zuo, M.; Kim, J.; Zhou, W.; Meng, X.; Yu, Q.; Sun, Z.; Wei, S.; Ye, J.; Wallace, G. G.; Officer, D. L.; Yamauchi, Y. Optimizing Electron Densities of Ni-N-C Complexes by Hybrid Coordination for Efficient Electrocatalytic CO_2 Reduction. *ChemSusChem* **2020**, *13* (5), 929–937.

(22) Levell, Z.; Yu, S.; Wang, R.; Liu, Y. What Is the "Other" Site in M–N–C? *J. Am. Chem. Soc.* **2024**, *147* (1), 603–609.

(23) Gao, D.; Liu, T.; Wang, G.; Bao, X. Structure Sensitivity in Single-Atom Catalysis toward CO2 Electroreduction. *ACS Energy Lett.* **2021**, *6* (2), 713–727.

(24) Bai, X.; Zhao, X.; Zhang, Y.; Ling, C.; Zhou, Y.; Wang, J.; Liu, Y. Dynamic Stability of Copper Single-Atom Catalysts under Working Conditions. *J. Am. Chem. Soc.* **2022**, *144* (37), 17140–17148.

(25) Yang, J.; Liu, W.; Xu, M.; Liu, X.; Qi, H.; Zhang, L.; Yang, X.; Niu, S.; Zhou, D.; Liu, Y.; others. Dynamic Behavior of Single-Atom Catalysts in Electrocatalysis: Identification of Cu-N_3 as an Active Site for the Oxygen Reduction Reaction. *J. Am. Chem. Soc.* **2021**, *143* (36), 14530–14539.

(26) Wang, Y.; Tang, Y.-J.; Zhou, K. Self-Adjusting Activity Induced by Intrinsic Reaction Intermediate in Fe–N–C Single-Atom Catalysts. *J. Am. Chem. Soc.* **2019**, *141* (36), 14115–14119.

(27) Li, P.; Jiao, Y.; Ruan, Y.; Fei, H.; Men, Y.; Guo, C.; Wu, Y.; Chen, S. Revealing the Role of Double-Layer Microenvironments in pH-Dependent Oxygen Reduction Activity over Metal-Nitrogen-Carbon Catalysts. *Nat. Commun.* **2023**, *14* (1), 6936.

(28) Tran, N. V.; Liu, J.; Li, S. Dynamic Adaptation of Active Site Driven by Dual-Side Adsorption in Single-Atomic Catalysts During CO_2 Electroreduction. *Angew. Chem. Int. Ed.* **2024**, *63* (52), e202411765.

(29) Qin, Y.; Zhao, W.; Xia, C.; Yu, L.-J.; Song, F.; Zhang, J.; Wu, T.; Cao, R.; Ding, S.; Xia, B. Y.; others. CO Intermediate-Assisted Dynamic Cu Sintering During Electrocatalytic CO_2 Reduction on Cu- N- C Catalysts. *Angew. Chem. Int. Ed.* **2024**, *63* (23), e202404763.

(30) Yang, N.; Peng, L.; Li, L.; Li, J.; Liao, Q.; Shao, M.; Wei, Z. Theoretically Probing the Possible Degradation Mechanisms of an FeNC Catalyst during the Oxygen Reduction Reaction. *Chem. Sci.* **2021**, *12* (37), 12476–12484.
(31) Bae, G.; Han, S.; Oh, H.-S.; Choi, C. H. Operando Stability of Single-atom Electrocatalysts. *Angewandte Chemie* **2023**, *135* (19), e202219227.
(32) Karapinar, D.; Huan, N. T.; Ranjbar Sahraie, N.; Li, J.; Wakerley, D.; Touati, N.; Zanna, S.; Taverna, D.; Galvão Tizei, L. H.; Zitolo, A. Electroreduction of CO_2 on Single-site Copper-nitrogen-doped Carbon Material: Selective Formation of Ethanol and Reversible Restructuration of the Metal Sites. *Angew. Chem. Int. Ed.* **2019**, *58* (42), 15098–15103.
(33) Zhang, Y.; Jiao, L.; Yang, W.; Xie, C.; Jiang, H.-L. Rational Fabrication of Low-Coordinate Single-Atom Ni Electrocatalysts by MOFs for Highly Selective CO_2 Reduction. *Angew. Chem. Int. Ed.* **2021**, *60* (14), 7607–7611.
(34) Gong, Y.-N.; Jiao, L.; Qian, Y.; Pan, C.-Y.; Zheng, L.; Cai, X.; Liu, B.; Yu, S.-H.; Jiang, H.-L. Regulating the Coordination Environment of MOF-Templated Single-Atom Nickel Electrocatalysts for Boosting CO_2 Reduction. *Angew. Chem. Int. Ed.* **2020**, *59* (7), 2705–2709.
(35) Yang, H. B.; Hung, S.-F.; Liu, S.; Yuan, K.; Miao, S.; Zhang, L.; Huang, X.; Wang, H.-Y.; Cai, W.; Chen, R.; others. Atomically Dispersed Ni (i) as the Active Site for Electrochemical CO_2 Reduction. *Nat. Energy* **2018**, *3* (2), 140–147.
(36) Su, P.; Iwase, K.; Harada, T.; Kamiya, K.; Nakanishi, S. Covalent Triazine Framework Modified with Coordinatively-Unsaturated Co or Ni Atoms for CO_2 Electrochemical Reduction. *Chem. Sci.* **2018**, *9* (16), 3941–3947.
(37) Wang, Y.; You, L.; Zhou, K. Origin of the N-Coordinated Single-Atom Ni Sites in Heterogeneous Electrocatalysts for CO_2 Reduction Reaction. *Chem. Sci.* **2021**, *12* (42), 14065–14073.
(38) Liu, S.; Yang, H. B.; Hung, S.-F.; Ding, J.; Cai, W.; Liu, L.; Gao, J.; Li, X.; Ren, X.; Kuang, Z.; Huang, Y.; Zhang, T.; Liu, B. Elucidating the Electrocatalytic CO_2 Reduction Reaction over a Model Single-Atom Nickel Catalyst. *Angew. Chem. Int. Ed.* **2020**, *59* (2), 798–803.
(39) Li, J.; Pršlja, P.; Shinagawa, T.; Martin Fernandez, A. J.; Krumeich, F.; Artyushkova, K.; Atanassov, P.; Zitolo, A.; Zhou, Y.; García-Muelas, R.; others. Volcano Trend in Electrocatalytic CO_2 Reduction Activity over Atomically Dispersed Metal Sites on Nitrogen-Doped Carbon. *ACS Catal.* **2019**, *9* (11), 10426–10439.
(40) Hossain, M. D.; Huang, Y.; Yu, T. H.; Goddard III, W. A.; Luo, Z. Reaction Mechanism and Kinetics for CO_2 Reduction on Nickel Single Atom Catalysts from Quantum Mechanics. *Nat. Commun.* **2020**, *11* (1), 2256.
(41) Zhao, X.; Liu, Y. Unveiling the Active Structure of Single Nickel Atom Catalysis: Critical Roles of Charge Capacity and Hydrogen Bonding. *J. Am. Chem. Soc.* **2020**, *142* (12), 5773–5777.
(42) Prslja, P.; López, N. Stability and Redispersion of Ni Nanoparticles Supported on N-Doped Carbons for the CO_2 Electrochemical Reduction. *ACS Catal.* **2021**, *11* (1), 88–94.

(43) Yan, C.; Li, H.; Ye, Y.; Wu, H.; Cai, F.; Si, R.; Xiao, J.; Miao, S.; Xie, S.; Yang, F.; Li, Y.; Wang, G.; Bao, X. Coordinatively Unsaturated Nickel–Nitrogen Sites towards Selective and High-Rate CO_2 Electroreduction. *Energy Environ. Sci.* **2018**, *11* (5), 1204–1210.
(44) Rong, X.; Wang, H.-J.; Lu, X.-L.; Si, R.; Lu, T.-B. Controlled Synthesis of a Vacancy-Defect Single-Atom Catalyst for Boosting CO_2 Electroreduction. *Angew. Chem. Int. Ed.* **2020**, *132* (5), 1977–1981.
(45) Zhao, H.; Cao, H.; Zhang, Z.; Wang, Y.-G. Modeling the Potential-Dependent Kinetics of CO2 Electroreduction on Single-Nickel Atom Catalysts with Explicit Solvation. *ACS Catal.* **2022**, *12* (18), 11380–11390.
(46) Zhang, X.; Wang, Y.; Gu, M.; Wang, M.; Zhang, Z.; Pan, W.; Jiang, Z.; Zheng, H.; Lucero, M.; Wang, H.; others. Molecular Engineering of Dispersed Nickel Phthalocyanines on Carbon Nanotubes for Selective CO_2 Reduction. *Nat. Energy* **2020**, *5* (9), 684–692.
(47) Li, C.; Ju, W.; Vijay, S.; Timoshenko, J.; Mou, K.; Cullen, D. A.; Yang, J.; Wang, X.; Pachfule, P.; Brückner, S.; Jeon, H. S.; Haase, F. T.; Tsang, S.-C.; Rettenmaier, C.; Chan, K.; Cuenya, B. R.; Thomas, A.; Strasser, P. Covalent Organic Framework (COF) Derived Ni-N-C Catalysts for Electrochemical CO_2 Reduction: Unraveling Fundamental Kinetic and Structural Parameters of the Active Sites. *Angew. Chem. Int. Ed.* **2022**, *61* (15), e202114707.
(48) Hu, K.; Ohto, T.; Nagata, Y.; Wakisaka, M.; Aoki, Y.; Fujita, J.; Ito, Y. Catalytic Activity of Graphene-Covered Non-Noble Metals Governed by Proton Penetration in Electrochemical Hydrogen Evolution Reaction. *Nat. Commun.* **2021**, *12* (1), 203.
(49) Dattila, F.; Seemakurthi, R. R.; Zhou, Y.; López, N. Modeling Operando Electrochemical CO_2 Reduction. *Chem. Rev.* **2022**, *122* (12), 11085–11130.
(50) Kozuch, S.; Shaik, S. A Combined Kinetic- Quantum Mechanical Model for Assessment of Catalytic Cycles: Application to Cross-Coupling and Heck Reactions. *J. Am. Chem. Soc.* **2006**, *128* (10), 3355–3365.
(51) Kozuch, S.; Shaik, S. How to Conceptualize Catalytic Cycles? The Energetic Span Model. *Acc. Chem. Res.* **2011**, *44* (2), 101–110.
(52) Razzaq, S.; Exner, K. S. Materials Screening by the Descriptor G Max (η): The Free-Energy Span Model in Electrocatalysis. *ACS Catal.* **2023**, *13* (3), 1740–1758.
(53) Campbell, C. T. The Degree of Rate Control: A Powerful Tool for Catalysis Research. *ACS Catal.***2017**, *7* (4), 2770–2779.
(54) Zhang, H.; An, P.; Zhou, W.; Guan, B. Y.; Zhang, P.; Dong, J.; Lou, X. W. (David). Dynamic Traction of Lattice-Confined Platinum Atoms into Mesoporous Carbon Matrix for Hydrogen Evolution Reaction. *Sci. Adv.* **2018**, *4* (1), eaao6657.
(55) Di Liberto, G.; Cipriano, L. A.; Pacchioni, G. Universal Principles for the Rational Design of Single Atom Electrocatalysts? Handle with Care. *ACS Catal.* **2022**, *12* (10), 5846–5856.
(56) Fung, V.; Hu, G.; Wu, Z.; Jiang, D. Descriptors for Hydrogen Evolution on Single Atom Catalysts in Nitrogen-Doped Graphene. *J. Phys. Chem. C* **2020**, *124* (36), 19571–19578.

(57) Xu, M.; Shu, Y.; Wang, X.; Chen, Y.; Xie, J.; Li, Y.; Dong, H. The Activity Origin of Two-Dimensional MN_4-Contained Periodical Macrocyclic Structures towards Electro-Catalytic Hydrogen Evolution. *J. Colloid Interface Sci.* **2025**, *686*, 1105–1113.
(58) Zhai, H.; Alexandrova, A. N. Ensemble-Average Representation of Pt Clusters in Conditions of Catalysis Accessed through GPU Accelerated Deep Neural Network Fitting Global Optimization. *J. Chem. Theory Comput.* **2016**, *12* (12), 6213–6226.
(59) Zhai, H.; Alexandrova, A. N. Fluxionality of Catalytic Clusters: When It Matters and How to Address It. *ACS Catal.* **2017**, *7* (3), 1905–1911.
(60) Zhang, Z.; Zandkarimi, B.; Alexandrova, A. N. Ensembles of Metastable States Govern Heterogeneous Catalysis on Dynamic Interfaces. *Acc. Chem. Res.* **2020**, *53* (2), 447–458.
(61) Liu, W.; Chen, Y.; Qi, H.; Zhang, L.; Yan, W.; Liu, X.; Yang, X.; Miao, S.; Wang, W.; Liu, C. A Durable Nickel Single-atom Catalyst for Hydrogenation Reactions and Cellulose Valorization under Harsh Conditions. *Angew. Chem. Int. Ed.* **2018**, *130* (24), 7189–7193.
(62) Qiu, Y.-Z.; Liu, X.-M.; Li, W.; Li, J.; Xiao, H. Transient Dangling Active Sites of Fe(III)−N−C Single-Atom Catalyst for Efficient Electrochemical CO_2 Reduction Reaction. *Angew. Chem. Int. Ed.* **2025**, *64* (16), e202424150.
(63) Zhang, Y.; Xia, J.; Jiang, B. REANN: A PyTorch-Based End-to-End Multi-Functional Deep Neural Network Package for Molecular, Reactive, and Periodic Systems. *J. Chem. Phys.* **2022**, *156* (11).
(64) Kresse, G.; Furthmüller, J. Efficiency of Ab-Initio Total Energy Calculations for Metals and Semiconductors Using a Plane-Wave Basis Set. *Comput. Mater. Sci.* **1996**, *6* (1), 15–50.
(65) Kresse, G.; Furthmüller, J. Efficient Iterative Schemes for Ab Initio Total-Energy Calculations Using a Plane-Wave Basis Set. *Phys. Rev. B Condens. Matter.* **1996**, *54* (16), 11169–11186.
(66) Perdew, J. P.; Burke, K.; Ernzerhof, M. Generalised Gradient Approximation Made Simple. *Phys. Rev. Lett. 77*, 3865 3868.
(67) Choi, J.; Chiu, S.; Banerjee, A.; Sacci, R. L.; Veith, G. M.; Stieber, C.; Hahn, C.; Alexandrova, A. N.; Morales-Guio, C. G. Corrosion and Enhanced Hydrogen Evolution in Electrochemical Reduction of Ammonium Carbamate on Transition Metal Surfaces. *J. Phys. Chem. Lett.* **2024**, 8007–8017.
(68) Zhang, Z.; Gee, W.; Sautet, P.; Alexandrova, A. N. H and CO Co-Induced Roughening of Cu Surface in CO_2 Electroreduction Conditions. *J. Am. Chem. Soc.***2024**. *146*(23), 16119−16127.
(69) Steinmann, S. N.; Michel, C.; Schwiedernoch, R.; Sautet, P. Impacts of Electrode Potentials and Solvents on the Electroreduction of CO_2 : A Comparison of Theoretical Approaches. *Phys. Chem. Chem. Phys.* **2015**, *17* (21), 13949–13963.
(70) Mahoney, M. W.; Drineas, P. CUR Matrix Decompositions for Improved Data Analysis. *Proc. Natl. Acad. Sci. U.S.A.* **2009**, *106* (3), 697–702.
(71) Bernstein, N.; Csányi, G.; Deringer, V. L. De Novo Exploration and Self-Guided Learning of Potential-Energy Surfaces. *Npj Comput. Mater.* **2019**, *5* (1), 99.

(72) Han, Y.; Xu, J.; Xie, W.; Wang, Z.; Hu, P. Unravelling the Impact of Metal Dopants and Oxygen Vacancies on Syngas Conversion over Oxides: A Machine Learning-Accelerated Study of CO Activation on Cr-Doped ZnO Surfaces. *ACS Catal.* **2023**, *13* (22), 15074–15086.
(73) Han, Y.; Xu, J.; Xie, W.; Wang, Z.; Hu, P. Comprehensive Study of Oxygen Vacancies on the Catalytic Performance of ZnO for CO/H_2 Activation Using Machine Learning-Accelerated First-Principles Simulations. *ACS Catal.* **2023**, *13* (8), 5104–5113.
(74) Xu, J.; Xie, W.; Han, Y.; Hu, P. Atomistic Insights into the Oxidation of Flat and Stepped Platinum Surfaces Using Large-Scale Machine Learning Potential-Based Grand-Canonical Monte Carlo. *ACS Catal.* **2022**, *12* (24), 14812–14824.
(75) Xu, J. *Generating Deep Potential with Python (GDPy)*; 2022.
(76) Kowalski, R. M.; Banerjee, A.; Yue, C.; Gracia, S. G.; Cheng, D.; Morales-Guio, C. G.; Sautet, P. Electroreduction of Captured CO_2 on Silver Catalysts: Influence of the Capture Agent and Proton Source. *J. Am. Chem. Soc.* **2024**, *146* (30), 20728–20741.
(77) Baxter, E. T.; Ha, M.-A.; Cass, A. C.; Alexandrova, A. N.; Anderson, S. L. Ethylene Dehydrogenation on Pt4,7,8 Clusters on Al_2O_3: Strong Cluster Size Dependence Linked to Preferred Catalyst Morphologies. *ACS Catal.* **2017**, *7* (5), 3322–3335.
(78) Sun, G.; Sautet, P. Metastable Structures in Cluster Catalysis from First-Principles: Structural Ensemble in Reaction Conditions and Metastability Triggered Reactivity. *J. Am. Chem. Soc.* **2018**, *140* (8), 2812–2820.
(79) Ha, M.-A.; Dadras, J.; Alexandrova, A. Rutile-Deposited Pt–Pd Clusters: A Hypothesis Regarding the Stability at 50/50 Ratio. *ACS Catal.* **2014**, *4* (10), 3570–3580.

Table of Contents